Journal of Materials Chemistry C

ROYAL SOCIETY OF CHEMISTRY

PAPER

View Article Online
View Journal | View Issue

Cite this: J. Mater. Chem. C, 2025, 13, 17120

Crystalline pseudorotaxane enabling dual-wavelength photothermal mechanical actuation†

Kuan-Hung Huang,[a] Hong-Kai Chang,[a] Meng-Che Tsai,[ac] Ting-Wei Liao,[ac] You-Ting Chen,[a] Chu-Liang Hsieh,[ac] Pei-Lin Chen,[b] Kai-Jen Chen *[ac] and Masaki Horie *[ac]

Received 30th May 2025,
Accepted 7th July 2025

DOI: 10.1039/d5tc02111a

rsc.li/materials-c

We report the synthesis and photothermal-mechanical conversion behavior of a photoresponsive pseudorotaxane comprising an ammonium salt bearing ferrocenyl and anthryl groups as the axle and dibenzo[24]crown-8 (DB24C8) as the macrocyclic ring. In the crystalline state, the pseudorotaxane exhibits notable void spaces around the ferrocene and anthryl substituents, with void volume increasing from 12.7% to 17.3% over the temperature range of −173 °C to 77 °C. The crystals display characteristic photoabsorption at 375 nm and 445 nm, attributed to the anthryl and ferrocenyl units, respectively, enabling efficient photothermal conversion. Upon incorporation into a poly(*n*-butyl methacrylate) (PBMA) matrix, the crystal-dispersed film undergoes significant temperature increases from 27 °C to 72 °C and 69 °C when irradiated at 375 nm and 445 nm, respectively, resulting in light-induced film expansion. This expansion translates into pronounced photoactuated lifting and bending motions, which are significantly greater than those observed in films containing only the axle or lacking the anthryl moiety. These findings demonstrate the utility of ferrocenyl–anthryl-functionalized crystalline pseudorotaxanes in the development of photomechanical materials, soft actuators, and optically responsive mechanical systems.

1. Introduction

Molecular machines and switches have been extensively studied for their capacity to manipulate molecular structures at the nanoscale in response to external stimuli.[1–8] Notably, mechanically interlocked rotaxanes and pseudorotaxanes—comprising ring and axle components—undergo relative positional changes upon exposure to stimuli such as light,[9–13] pH shifts,[14] thermal input,[15,16] and chemical signals.[5,7] Due to their structural adaptability during such responses, these systems can transmit forces,[4,17] motions,[5,18] and energy[4,19] both within individual molecules and across molecular assemblies, depending on the specific characteristics of the supramolecular architecture. To date, most investigations of molecular machines have been conducted in solution,[20–22] where molecular alignment is inherently absent. In contrast, in the crystalline state, molecules are precisely aligned, oriented, and regularly spaced, enabling concerted molecular motions that can produce macroscopic mechanical effects.[1,2,23–25]

Organic photochemical and thermal reactions capable of generating mechanical motion on scales from nanometers to millimeters have attracted significant attention due to the diverse range of molecular systems and available reaction pathways.[6,9,26,27] These stimuli-responsive systems offer notable advantages, such as rapid response[6,18,28,29] and high elastic modulus,[6] positioning molecular crystals as promising candidates for photo- and thermomechanical actuators. Stimulus-induced transformations in these crystals can generate various mechanical motions, including expansion,[23,30] bending,[27,31] twisting,[18,31] and curling.[32] In several cases, structural changes associated with these dynamic responses have been elucidated by single-crystal X-ray crystallography.[23] Crystalline molecular systems also offer significant potential in applications ranging from optoelectronics,[33,34] rotors,[29,35] and sensors,[36] to drug delivery,[25] and catalysis.[37,38] This versatility stems from the high density and precise spatial organization of functional components within crystals. These properties are generally difficult to achieve in dilute solutions or thin surface-bound assemblies. While these advantages are notable, most molecular crystals exhibit dense packing, which often limits the free volume necessary for dynamic molecular motion.[39] Therefore, careful

[a] Department of Chemical Engineering, National Tsing Hua University, 101, Section 2, Kuang-Fu Road, Hsinchu 30013, Taiwan
[b] Instrumentation Center, National Tsing Hua University, 101, Section 2, Kuang-Fu Road, Hsinchu 30013, Taiwan
[c] Research Institute for Electronic Science (RIES), Hokkaido University, N21W10, Kita-Ward, Sapporo 001-0021, Japan. E-mail: kjchen@es.hokudai.ac.jp, mhorie@es.hokudai.ac.jp

† Electronic supplementary information (ESI) available: Detailed characterization, crystallographic data, fundamental characteristics, and movies of thermography and film bending. CCDC 2452984. For ESI and crystallographic data in CIF or other electronic format see DOI: https://doi.org/10.1039/d5tc02111a

molecular design and advanced crystal engineering are essential to realizing functional, solid-state dynamic molecular machines.

We have synthesized a range of pseudorotaxanes and complexes consisting of dibenzo-crown ethers (host molecules) and functionalized ammonium salts (guest molecules), and have investigated their structural transformations and dynamic behaviors in response to external stimuli.[1,2] For example, crystals composed of dibenzo[24]crown-8 ether (DB24C8) and ferrocene-containing ammonium salts exhibited reversible crystal-to-crystal phase transitions and morphological changes upon heating and photoirradiation.[40,41] In another system, crystals formed from dibenzo-crown ethers and azobenzene-functionalized ammonium salts exhibited reversible bending motions upon photoirradiation, driven by *cis–trans* isomerization of the azobenzene moiety induced by light and heat.[42–44] Within these assemblies, each molecular component plays a distinct role. The dibenzo-crown ether serves as the host framework, offering sufficient spatial freedom to accommodate guest mobility.[45] In contrast, the functional ammonium salts act as transducers, converting absorbed light energy into mechanical motion. Under certain conditions, intermolecular interactions can immobilize the guest species, resulting in rigid structures that inhibit motion.[42–44] To overcome this limitation, structural modifications, such as introducing different functional substituents or extending the axle length, are essential for enhancing molecular mobility within the crystalline matrix.

Anthracene and its derivatives are recognized for their high planarity, extended π-conjugation, and strong fluorescence.[46–49] These characteristics have been widely utilized in the development of luminescent materials and organic semiconductors. In addition, certain derivatives undergo [4+4] photodimerization in the crystalline state, which can induce photosalient effects.[50–53] For example, bis-*o*-carborane-substituted anthracene undergoes photodimerization, leading to macroscopic mechanical responses in the crystal such as cracking, debris formation, and jumping, accompanied by decolorization. These phenomena have been observed using fluorescence microscopy, and the molecular structures before and after photodimerization have been determined by single-crystal X-ray crystallography.[51] Anthryl groups have also been incorporated into rotaxanes and pseudorotaxanes, enabling photocycloaddition and functioning as photoluminescent units in solution.[54–56] Moreover, anthracene-containing compounds have been investigated in thin-film systems.[54,55] Despite these advances, no studies have yet reported the functionalization of anthracene units within single-crystal pseudorotaxanes.

Soft actuators composed of flexible polymers, such as poly(*n*-butyl methacrylate) (PBMA)[57] and polyurethane,[58] offer several advantages, including high flexibility, adaptability, and reconfigurability, which resemble properties found in biological systems.[59,60] These features support a wide range of applications, such as soft electronics, surgical tools, drug delivery systems, artificial organs, and prosthetic devices.[60,61] The integration of intelligent materials into soft actuator systems expands their functional capabilities, enabling changes in structure, macroscopic behavior, and shape in response to external stimuli including electric fields, thermal input, and light.[60,62] Organic chromophores are commonly used

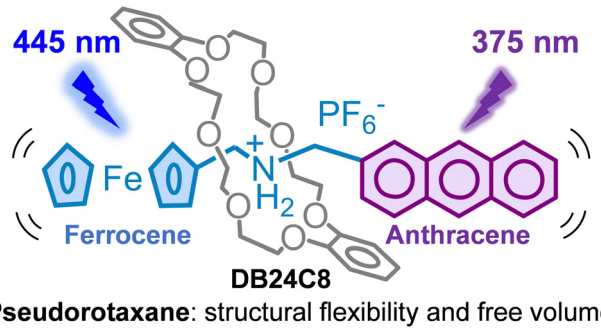

Fig. 1 Schematic of ferrocenyl- and anthryl-containing pseudorotaxane for photoinduced motion.

in photothermal conversion materials due to their tunable structures, favorable photophysical properties, strong absorption in the near-infrared region, excellent biocompatibility, and high photostability.[63–65] Soft polymers serve as effective host matrices due to their intrinsic elasticity and compatibility with photoresponsive guest molecules, which together facilitate reversible mechanical deformation. In previous work, we developed photoresponsive soft actuators incorporating ferrocene-based and dithienylethene chromophores embedded in PBMA.[57,66] These actuators exhibited light-induced bending, vertical lifting motions, and self-healing capabilities following mechanical damage.

In this study, we report a novel pseudorotaxane composed of an ammonium salt bearing ferrocenyl and anthryl groups as the axle component and dibenzo[24]crown-8 (DB24C8) as the ring component, which provides flexibility and internal free volume (Fig. 1). We investigate structural changes in the single-crystal state, where the ferrocenyl and anthryl moieties exhibit distinct absorption at 445 nm and 375 nm, respectively, enabling efficient photothermal conversion. Incorporation of the crystals into a PBMA matrix results in pronounced light-induced lifting and bending motions. The photomechanical response exceeds that of films composed solely of the axle molecule or those lacking the anthryl unit. These findings demonstrate the potential of crystalline pseudorotaxanes incorporating functional chromophores for applications in photomechanical materials and soft actuation systems.

2. Results and discussion

2.1. Synthesis and characterization

Scheme 1 illustrates the synthesis of pseudorotaxane **PR1**, which consists of a ferrocenyl- and anthryl-functionalized ammonium hexafluorophosphate (PF_6^-) axle (**A1**) and DB24C8. The axle molecule **A1** was synthesized *via* condensation of anthracene-2-carbaldehyde with ferrocenemethylamine, followed by hydrogenation and protonation. Single crystals of **PR1** were obtained by vapor diffusion of diethyl ether (Et_2O) into a dichloromethane–acetone solution containing a mixture of **A1** and DB24C8. Obtained compounds were confirmed by ^{1}H NMR and mass spectroscopies (Fig. S1–S11, ESI†). For comparative analysis, the previously reported pseudorotaxane **PR2**,[40,41] bearing a tolyl substituent, and its corresponding axle **A2** are also examined.

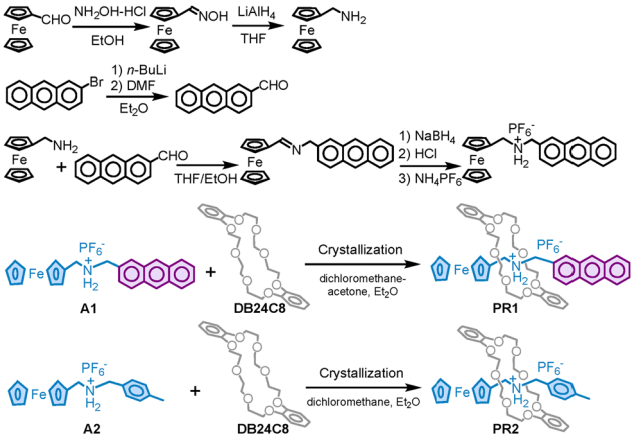

Scheme 1 Synthesis of **PR1** and **PR2**.

The structural changes of **PR1** at various temperatures were analyzed by single-crystal X-ray crystallography (Fig. 2, 3 and Fig. S12, S13, Tables S3, S4, ESI†). Due to substantial deterioration in data quality above 77 °C (350 K), detailed structural analysis is based on the crystallographic data obtained below 47 °C (320 K). Fig. 2a–3c present the molecular structure of **PR1**, a detailed view of the ferrocenyl unit, and a summary of the intra- and intermolecular interactions, along with temperature-dependent structural changes. **PR1** is primarily stabilized by [N–H···O] and [C–H···O] hydrogen bonds (2.43–3.06 Å) between the ammonium N–H or N–CH_2 protons and the oxygen atoms of DB24C8. An intramolecular [π···π] interaction is observed between one catechol unit of DB24C8 and the ferrocenyl moiety of **A1**, with the centroid–centroid distance increasing from 3.94 Å at −173 °C to 3.98 Å at 24 °C (Fig. 2a). At −173 °C, the two cyclopentadienyl (Cp) rings of the ferrocenyl group adopt a nearly eclipsed conformation with a dihedral angle of 0.1°. Upon heating to 24 °C, this angle increases to 5°, suggesting a slight rotation that reduces steric repulsion between Cp-ring hydrogen atoms. As a result, the Cp–Cp distance decreases from 3.29 Å (Fig. 2b). At 77 °C, further conformational changes are observed, with partial collapse of the ferrocenyl units, indicating increased conformational freedom of the ferrocene group.

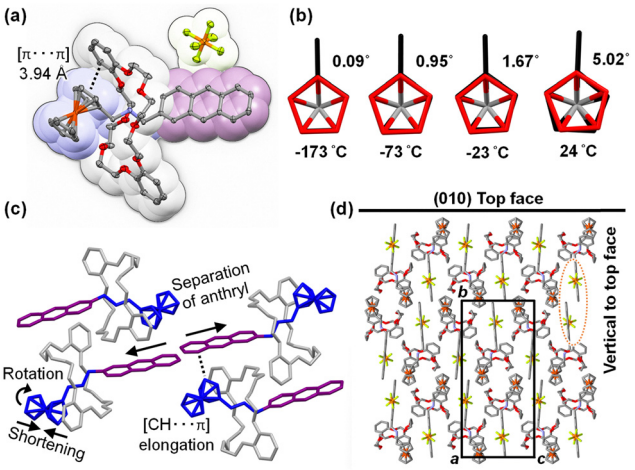

Fig. 2 (a) Molecular structure of **PR1** determined by single-crystal X-ray crystallography at −173 °C. (b) Top view of the ferrocenyl group at various temperatures. (c) Schematic representation of molecular motion upon heating. (d) Molecular packing at −173 °C.

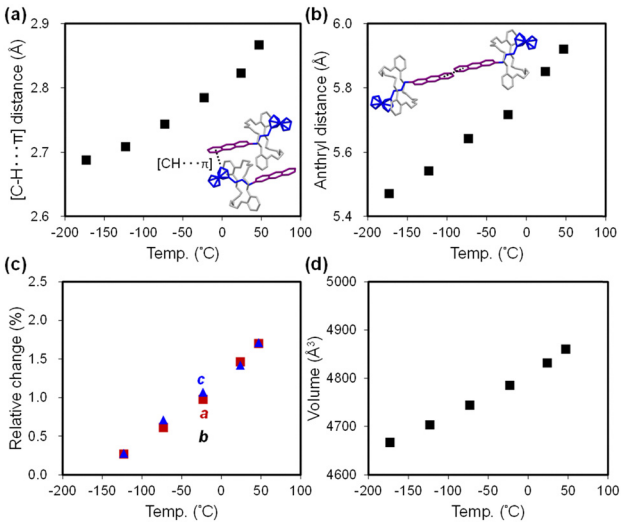

Fig. 3 Temperature dependence of **PR1**: (a) [C–H···π] interaction distance, (b) anthryl–anthryl distance, (c) relative changes in unit cell parameters, and (d) unit cell volume.

Intermolecular interactions are also temperature dependent. A [C–H···π] interaction is observed between the anthryl unit and a neighboring ferrocenyl group, with the interaction distance increasing from 2.69 Å to 2.87 Å between −173 °C and 47 °C (Fig. 2c and 3a). Additionally, the distance between anthryl moieties in adjacent molecules increases by 8.2%, from 5.47 Å to 5.92 Å over the same temperature range (Fig. 2c and 3b). This increase precludes π–π stacking and photocyclization in the crystalline state.

Crystal packing analysis (Fig. 2d) reveals that the top surface corresponds to the (010) plane, with the crystal extending along the *a*- and *c*-axes, while the thickness aligns with the *b*-axis. Thus, the relationship between macroscopic crystal deformation and molecular-level packing changes is considered. Fig. 3c and d illustrate temperature-dependent variations in unit cell parameters and volume. Between −173 °C and 47 °C, the *a*- and *c*-axes expand by 1.7%, whereas the *b*-axis increases only marginally by 0.6%. The overall volume increase is therefore primarily due to elongation along the *a*- and *c*-axes, attributed to enhanced ferrocenyl mobility at elevated temperatures. As noted earlier, weakening of [C–H···π] interactions facilitates this mobility and contributes to crystal plane expansion. Although the anthryl group remains conformationally rigid, the increasing intermolecular distance along the *b*-axis slightly contributes to overall crystal expansion.

The volumetric thermal expansion coefficient (α_v) is estimated to be 1.88 × 10^{-4} K^{-1}, exceeding values typically reported for crystalline organic compounds[67] and metal–organic materials.[68] This temperature-dependent molecular motion and anisotropic expansion play a key role in the photothermal–mechanical conversion discussed in subsequent sections.

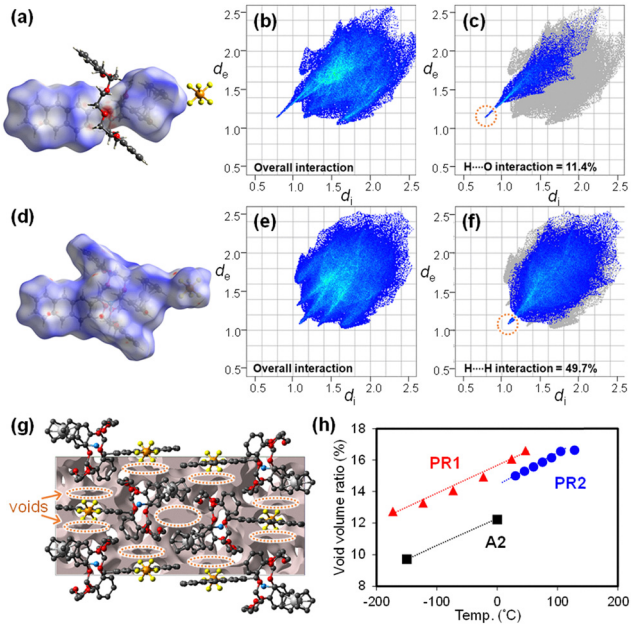

Fig. 4 (a) Hirshfeld plot of d_{norm} for the axle molecule in **PR1** at −173 °C. (b) 2D fingerprint plots of overall interactions and (c) dominated interactions for the axle molecule in **PR1** at −173 °C. (d) Hirshfeld plot of d_{norm} for **PR1** at −173 °C. (e) 2D fingerprint plots of overall interactions and (f) dominated interaction in **PR1** at −173 °C. (g) Graphical representation of voids in the crystal packing of **PR1** at 47 °C. (h) Temperature dependence of the void volume ratio for **PR1**, **PR2**, and **A2** with trend lines.

Hirshfeld surface and crystal void analyses are performed using CrystalExplorer version 21.5[69] to visualize intra- and intermolecular interactions in **PR1** (Fig. 4). The Hirshfeld surface is generated by partitioning the crystal space into distinct regions based on proximity to atoms. The parameters d_e and d_i represent the distances from a point on the surface to the nearest nucleus outside and inside the surface, respectively. The normalized contact distance (d_{norm}) is used to highlight intermolecular interactions, with its color scale reflecting deviations from van der Waals radii.

In the interaction between **A1** and DB24C8 (Fig. 4a), intense red regions are observed around the protonated amino group of the cation and the oxygen atoms of DB24C8, indicating strong [N–H···O] hydrogen bonding. Fig. 4b presents the 2D fingerprint plot of the axle molecule (also shown in Fig. S15–S18, ESI†), where sharp spikes correspond to significant interactions.[70,71] The dominant contribution arises from O···H/H···O contacts ($d_i + d_e \sim 2.0$ Å), consistent with [N–H···O] interactions (Fig. 4c). White patches between the catechol and ferrocenyl units indicate weak π–π interactions. The largest contribution in the fingerprint plot is from H···H contacts (52.7%), concentrated around $d_i = d_e \approx 1.2$ Å, largely arising from π-stacking tendencies between the ferrocenyl and catechol groups.

For intermolecular interactions between **PR1** molecules (Fig. 4d), the fingerprint plots indicate that H···H contacts dominate ($d_i + d_e \sim 2.2$ Å), corresponding to [C–H···π] interactions between ferrocenyl and anthryl groups (Fig. 4e, f, and Fig. S19–S22, ESI†). With increasing temperature, the [N–H···O] intramolecular interactions between the axle and ring remain essentially constant ($d_i + d_e \sim 2.0$ Å), while the [C–H···π] interactions between **PR1** molecules weaken, increasing the sum of distances to approximately 2.4 Å.

Fig. 4g (also shown in Fig. S23, ESI†) shows the crystal void distribution in the unit cell of **PR1**. Fig. 4h plots the temperature-dependent void volume for **PR1** in comparison with **PR2** and **A2**. Voids are primarily localized around the ferrocenyl and anthryl groups. The void volume of **PR1** increases linearly with temperature, rising from 12.7% at −173 °C to 17.3% at 77 °C, closely following the unit cell volume expansion trend (Fig. 3d). Notably, the void volume of **PR1** is approximately 1.5% greater than that of **PR2** and 3.5% greater than that of its axle molecule **A2**. These values also exceed the typical void fraction for organic crystals (7.3–8.6%).[72,73] These results suggest that incorporation of both the pseudorotaxane structure and ferrocenyl/anthryl functionalities effectively enhances free volume within the crystal, which is considered advantageous for promoting photomechanical conversion.

2.2. Film preparation and characterization

PR1 was incorporated into PBMA to prepare free-standing films, as illustrated in Scheme 2. Single crystals of **PR1** were ground and dispersed in 300 μL of a PBMA solution in diethyl ether. The concentration of **PR1** in PBMA was adjusted to 7 mol% (35 wt%), as summarized in Table S6 (ESI†). The dispersion was cast onto a PTFE film placed on a glass slide and allowed to dry. The dried film was then sandwiched between another PTFE film and a 70 μm spacer, followed by hot pressing at 50 °C. After molding, the film was peeled off, cut into 1 × 1 mm^2 pieces, and designated as **Cr.PR1-PBMA**. For comparison, a PBMA film containing crystalline **PR2** (**Cr.PR2-PBMA**) was prepared using the same procedure. In addition, a film referred to as **PR1-PBMA** was fabricated by casting a cosolvent mixture of chloroform and acetone containing **A1**, DB24C8, and PBMA in a molar ratio of 7 : 7 : 86 (19 : 16 : 65 wt%). According to the ^{1}H NMR spectra (Fig. S11, ESI†), the complexation ratio of **PR1** in $CDCl_3$: acetone-d_6 (70 : 30, vol/vol) is estimated to be approximately 60 mol% (**PR1**-complex : **PR1**-added), suggesting that **PR1** is the predominant species in the film. For further comparison, a film doped with **A1** alone is prepared and referred to as **A1-PBMA**.

The surface morphology of the films was analyzed using polarized optical microscopy, scanning electron microscopy

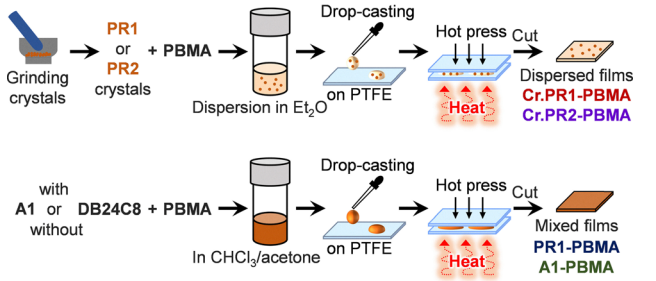

Scheme 2 Preparation of PBMA films.

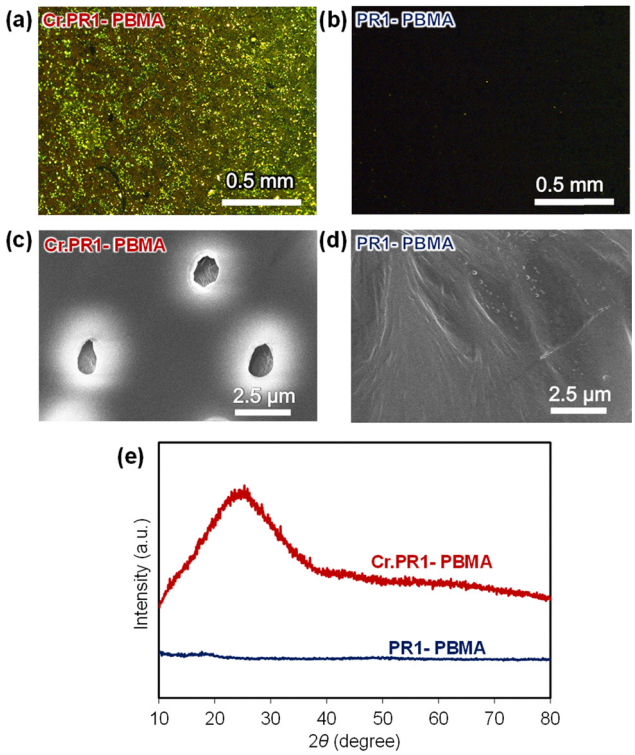

Fig. 5 Polarized optical micrographs of (a) **Cr.PR1-PBMA** and (b) **PR1-PBMA**. SEM images of (c) **Cr.PR1-PBMA** and (d) **PR1-PBMA**. (e) XRD patterns of the films.

(SEM), and two-dimensional X-ray diffraction (2D XRD). Fig. 5a and b present polarized optical micrographs of crystal-dispersed **Cr.PR1-PBMA** and pseudorotaxane-containing **PR1-PBMA.** Under polarized light, **Cr.PR1-PBMA** exhibits interference colors, indicating the presence of microcrystalline domains, whereas **PR1-PBMA** appears dark, suggesting an amorphous and uniform distribution within the PBMA matrix. A similar trend is observed for other films: **Cr.PR2-PBMA** contains microcrystals, while **A1-PBMA** appears uniformly dark (Fig. S24–S27, ESI†).

SEM images of **Cr.PR1-PBMA** and **PR1-PBMA** (Fig. 5c and d; see also Fig. S28–S31, ESI†) reveal clear morphological differences. **Cr.PR1-PBMA** displays evenly distributed microcrystals approximately 1–2 μm in diameter, whereas **PR1-PBMA** shows minimal evidence of crystallization. Elemental distribution is further confirmed by energy-dispersive X-ray spectroscopy (EDX). Elemental mappings of Fe, P, and F confirm the presence of **PR1** ($C_{50}H_{56}F_6FeNO_8P$) in both **Cr.PR1-PBMA** and **PR1-PBMA.**

Fig. 5e shows the 2D XRD patterns of **Cr.PR1-PBMA** and **PR1-PBMA.** A broad diffraction peak appears at 2θ = 20–30° for **Cr.PR1-PBMA**, indicative of crystalline domains, while **PR1-PBMA** exhibits no such diffraction, confirming its amorphous nature. Similar diffraction behavior is observed for **Cr.PR2-PBMA** and **A1-PBMA** (Fig. S32, ESI†).

2.3. Photothermal conversion

Fig. 6a presents the UV-vis absorption spectrum of **PR1** in acetone, showing three absorption peaks at λ_{abs} = 340, 358, and 378 nm, corresponding to the anthryl moiety, and a weak absorption at λ_{abs} = 440 nm, attributed to the ferrocenyl group. The photoluminescence (PL) spectrum of **PR1** in acetone (Fig. S33, ESI†) exhibits an emission band at λ_{PL} = 432 nm, with a PL quantum yield (PLQY) below 1% (Table S7, ESI†). This value is considerably lower than those reported for anthracene (36%), polycarbosilane grafted with 9-ethylanthracene (66–80%), and terphenyl–anthryl–pyrenoimidazole derivatives (89%).[74–76] The PL quenching is possibly attributed to photoinduced electron transfer from the anthryl to the ferrocenyl unit, which facilitates non-radiative decay and is favorable for photothermal conversion.[77]

Based on the absorption characteristics of **PR1**, the 375-nm and 445-nm lasers were selected for further investigation. Fig. 6b shows thermographic images of the **Cr.PR1-PBMA** film under continuous laser irradiation at 375 nm (15 mW cm^{-2}) or 445 nm (61 mW cm^{-2}). The surface temperature increases from 27 °C to 72 °C and 69 °C, respectively. The time-dependent temperature profile under 375-nm irradiation with an off–on–off cycle is shown in Fig. 6c for **Cr.PR1-PBMA** and comparison films. As summarized in Table 1, **Cr.PR1-PBMA** reaches the highest temperature (72 °C), followed by **PR1-PBMA** (65 °C), **A1-PBMA**

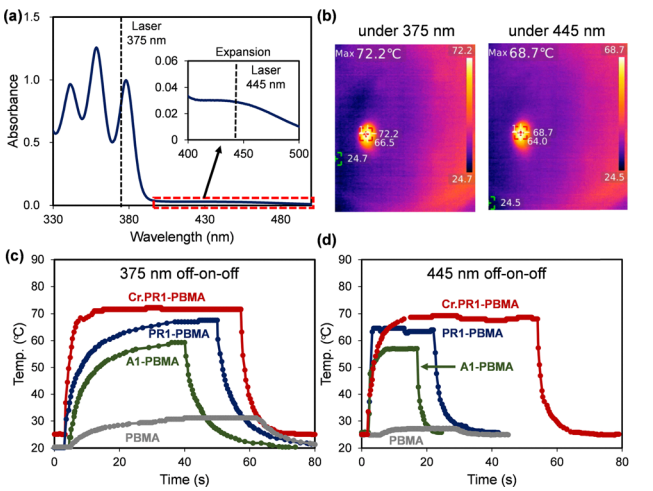

Fig. 6 (a) UV-vis absorption spectrum of **PR1** in acetone solution, with laser wavelengths at 375 nm and 445 nm indicated. (b) Thermographic images of **Cr.PR1-PBMA** with irradiation at 375 nm (15 mW cm^{-2}) or 445 nm (61 mW cm^{-2}). Time-dependent temperature profiles of PBMA films under (c) 375 nm irradiation (15 mW cm^{-2}) and (d) 445 nm irradiation (61 mW cm^{-2}).

Table 1 Summary of photothermal conversion of PBMA films

Films[a]	Laser (nm)	Power (mW cm^{-2})	Weight (mg)	Max. temp. (°C)	τ (s)
Cr.PR1-PBMA	375	15	0.6	72	3.1
	445	61	0.6	69	1.8
PR1-PBMA	375	15	0.68	65	4.7
	445	61	0.72	64	2.1
A1-PBMA	375	15	0.49	57	4.2
	445	61	0.42	57	1.5
Fc-PBMA[57]	445	61	0.41	65	2.4

[a] Comprising 7 mol% of chromophore in PBMA.

(57 °C), and PBMA alone (31 °C). A similar trend is observed under 445-nm irradiation (Fig. 6d). After the light source is switched off, the temperature returns to ambient (20–25 °C) within 15–20 s.

Based on the initial temperature decay profile, the time constant (τ) for each film was calculated and summarized in Table 1, as well as in Fig. S35 (ESI†). The τ values range from 1.5 to 4.7 s, which are approximately two orders of magnitude shorter than previously reported values ($\sim$230 s) for conjugated oligoelectrolytes.[78] This rapid photothermal response is considered advantageous for efficient photomechanical conversion.

Dynamic mechanical analysis (DMA) was performed to evaluate the thermal behavior of the films. The DMA profiles of **A1-PBMA** and **PR1-PBMA** reveal glass transition temperatures (T_g) of 25 °C and 47 °C, respectively, with a common tan δ peak at 57 °C (Fig. S37, ESI†). The T_g corresponds to the onset of local segmental motion of the polymer chains, while the tan δ peak reflects larger-scale molecular mobility within the network. These results indicate that the films maintain a rubbery state within the operational temperature range, and that laser-induced heating increases polymer chain mobility, facilitating deformation. Additionally, **PR1-PBMA** remains stable at room temperature, resisting deformation, but undergoes a smooth transition to a flexible state upon reaching temperatures beyond T_g. The coefficient of thermal expansion (CTE) was determined to be 5.7×10^{-3} for **A1-PBMA** and 5.8×10^{-3} for **PR1-PBMA** in the temperature range of 50–75 °C, as measured by laser scanning confocal microscopy. Previous studies report that the CTE of PBMA above its T_g is approximately 14 times greater than below T_g.[79] These findings support the conclusion that film deformation arises from photoabsorption by the anthryl or ferrocenyl groups, followed by photothermal conversion and thermal activation of polymer chain mobility.

2.4. Photoinduced deformation and mechanical output

Photoinduced deformation of chromophore-doped PBMA films (**Cr.PR1-PBMA**, **PR1-PBMA**, and **A1-PBMA**) and single crystals of **PR1** and **PR2** was investigated using optical and confocal laser microscopy under 375 nm or 445 nm irradiation (Fig. 7a–c and Fig. S38–S40, ESI†). Upon 375-nm laser irradiation at 28 mW cm^{-2}, **Cr.PR1-PBMA** expands in width, length, and thickness by 0.8%, 1.0%, and 7.8%, respectively (Fig. 7a). Similarly, under 445-nm irradiation at 40 mW cm^{-2}, the corresponding expansion values are 0.6%, 0.5%, and 5.7%. After cessation of irradiation, the film rapidly contracts to its original dimensions. Comparable photoinduced expansion is observed for the other PBMA-based films and for the **PR1** and **PR2** single crystals. The relative area changes of the top surfaces of the films and crystals under both wavelengths are summarized in Fig. 7b and c. In all cases, the extent of deformation follows the trend: **PR1** crystal $\approx$ **Cr.PR1-PBMA** > **PR1-PBMA** > **A1-PBMA** > **PR2** crystal. The larger deformation observed under 375-nm irradiation compared to 445-nm is attributed to the superior photothermal conversion efficiency of the anthryl group relative to the ferrocenyl group. Moreover, the PBMA film containing the pseudorotaxane (**PR1**) shows greater deformation than the film containing only the axle molecule

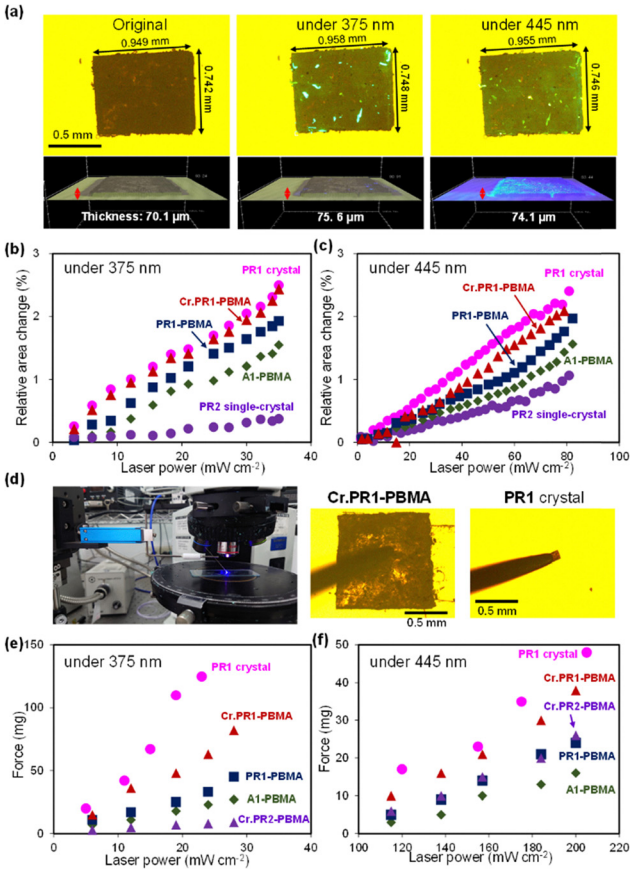

Fig. 7 (a) Optical and confocal micrographs of **Cr.PR1-PBMA** without and under 375-nm (28 mW cm^{-2}) or 445-nm (40 mW cm^{-2}) laser irradiation. Photoinduced relative area change under (b) 375-nm laser and (c) 445-nm laser irradiation at different laser powers. (d) Photograph and optical micrographs of force output measurement using a μ-force analyzer. μ-Force analyzer signal response under (e) 375-nm and (f) 445-nm laser irradiation.

(**A1**), highlighting the cooperative effect of the pseudorotaxane structure in enhancing mechanical output. The significantly enhanced mechanical output of **Cr.PR1-PBMA** is likely due to the increased free volume induced by the crown ether component, which facilitates greater molecular mobility and contributes to the cooperative effect.

The mechanical forces generated by the **PR1** crystal, **Cr.PR1-PBMA** film, and **PR1-PBMA** film on a glass substrate are measured using a microforce analyzer under focused 445-nm laser irradiation (Fig. 7d–f and Fig. S42, S43, ESI†). Upon exposure to 445-nm light at 0.18 W cm^{-2}, both the **PR1** crystal and **Cr.PR1-PBMA** film generate lifting forces of approximately 100 mg. In contrast, the **PR1-PBMA** film exhibits a lower lifting force of approximately 40 mg under slightly higher irradiation intensity (0.23 W cm^{-2}). The sample thicknesses are 51 μm for the crystal, 20 μm for **Cr.PR1-PBMA**, and 21 μm for **PR1-PBMA**.

The mechanical output of the films and crystals was evaluated using a microforce analyzer equipped with a strain gauge connected to a cantilever, which was placed in contact with the surface of the PBMA films or a single **PR1** crystal oriented on the (010) plane (Fig. 7d). For PBMA-based films, a double-layer structure comprising the PBMA film and a transparent cellophane

tape as a passive layer was employed to ensure stable force measurement. The generated upward force was recorded under 375-nm or 445-nm laser irradiation at varying power, with the laser alternately switched on and off (Fig. 7e, f and Fig. S42, S43, ESI†). The measured force is found to be proportional to the laser power. Among all samples, the **PR1** single crystal produces the highest mechanical output under both irradiation conditions, which is attributed to its high density and ordered molecular packing.

Under 375-nm irradiation at 23 mW cm^{-2}, the **PR1** crystal generates a force of 125 milligram-force (mgf, 1 mgf = 9.81×10^{-6} N), corresponding to approximately 67 000 times its own weight. Under 445-nm irradiation at 236 mW cm^{-2}, the force reaches 53 mgf, or about 23 000 times its own weight (Fig. S42c and d, ESI†). These values represent the highest mechanical output reported in our studies to date.[80,81] Furthermore, the **PR1** crystal demonstrates excellent reversibility, undergoing repeated expansion and contraction over more than 50 on/off cycles without significant performance degradation (Fig. S42e, ESI†).

Next, the force outputs of various double-layer PBMA films and single crystals are compared under 375-nm or 445-nm laser irradiation (Fig. 7e, f and Fig. S43a, b, ESI†). Under 375-nm irradiation, the force output follows the order: **PR1** crystal > **Cr.PR1-PBMA** > **PR1-PBMA** > **A1-PBMA** > **Cr.PR2-PBMA**. Under 445-nm irradiation, the order is: **PR1** crystal > **Cr.PR1-PBMA** > **Cr.PR2-PBMA** ≈ **PR1-PBMA** > **A1-PBMA**. Among the PBMA-based films, **Cr.PR1-PBMA** exhibits the highest mechanical output under both wavelengths. This performance is attributed to the photothermal expansion of the embedded microcrystals and the combined light absorption of the anthryl and ferrocenyl moieties at 375 nm and 445 nm, respectively. Notably, **Cr.PR1-PBMA**, which incorporates DB24C8, generates a significantly greater force than **A1-PBMA**, which lacks the crown ether. This enhancement suggests that the pseudorotaxane structure contributes to efficient deformation by spatially isolating **A1** molecules within the PBMA matrix and promoting cooperative motion. Repeatability testing on **PR1-PBMA** under repeated laser on/off cycling confirms stable and reversible mechanical response over more than 30 cycles (Fig. S43e, ESI†), supporting its durability for repeated actuation applications.

Photoinduced bending of the double-layer films was examined under laser irradiation (Fig. 8a). In this configuration, the crystal-dispersed active layer expands upon light exposure, while the attached passive layer restricts three-dimensional expansion, resulting in two-dimensional deformation and macroscopic bending of the film. Fig. 8b shows side-view optical microscopy images of **Cr.PR1-PBMA** with the passive layer. The film displays a larger bending displacement of 0.17 mm under 375-nm irradiation compared to 0.11 mm under 445-nm irradiation.

Time-dependent displacement profiles under repeated on/off laser cycles are presented in Fig. 8c for various PBMA-based films. Under 375-nm irradiation, **Cr.PR1-PBMA** achieves the largest displacement, reaching a maximum within 5.3 s and returning to its original position within 4.8 s after irradiation ceases. The displacement magnitudes follow the order: **Cr.PR1-PBMA** > **PR1-PBMA** > **A1-PBMA**. In contrast, **Cr.PR2-PBMA** shows minimal response due to its poor absorption at this wavelength.

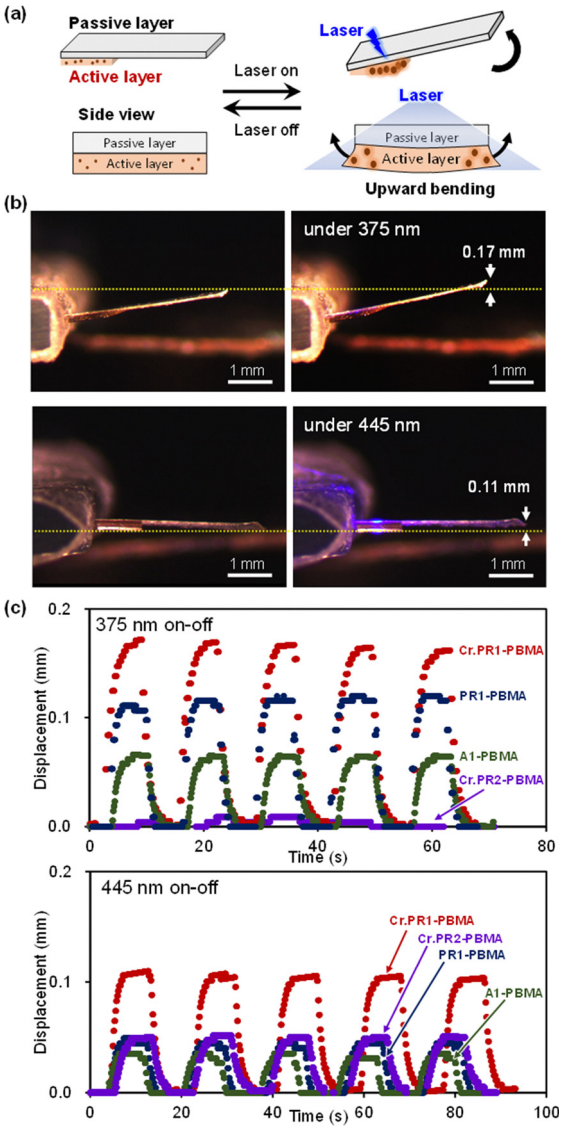

Fig. 8 (a) Illustration of the bending motion of a double-layer film. (b) Photographs of **Cr.PR1-PBMA** without and with 375-nm (4.9 mW cm^{-2}) or 445-nm (13 mW cm^{-2}) laser irradiation. (c) Time-dependent displacement of PBMA films under 375-nm (4.9 mW cm^{-2}) and 445-nm (13 mW cm^{-2}) laser irradiation.

Under 445-nm irradiation, **Cr.PR1-PBMA** again exhibits the greatest displacement, with expansion occurring within 2.4 s and recovery within 3.9 s. Other PBMA-based films also show light-induced bending, though the magnitude and response speed are lower compared to **Cr.PR1-PBMA**.

3. Conclusions

In this study, we have developed a photoresponsive pseudorotaxane composed of anthryl and ferrocenyl moieties as axle components and a crown ether as the ring. The incorporation of anthryl and ferrocenyl groups increases the internal free volume of the crystal, facilitating structural deformation, and enhances UV-vis absorption, enabling activation at both

375 nm and 445 nm. The single crystal of **PR1** exhibits the highest photoinduced mechanical output among the materials studied and maintains high performance even when embedded in a soft PBMA matrix. This crystal-based molecular system shows rapid responsiveness and excellent stability, making it a promising photoactuator. These findings provide insights into the design of photoresponsive materials and offer guiding principles for the development of next-generation functional systems. The moldability of the films into various forms further broadens their application potential. This approach enables the realization of light-driven, electricity-free devices and energy-efficient mechanical systems, with potential contributions to emerging fields such as soft robotics and adaptive materials.

4. Experimental section

4.1. Materials and general methods

PR2 was synthesized according to a previously reported procedure.[40] Poly(*n*-butyl methacrylate) (PBMA; number-average molecular weight = 337 000 g mol^{-1}, intrinsic viscosity = 0.47–0.56 dL g^{-1}), sodium acetate (CH_3COONa) and dibenzo[24]crown-8 (DB24C8) were purchased from Sigma-Aldrich. *n*-Butyllithium (*n*-BuLi), hydroxylamine hydrochloride, 3 Å molecular sieves, ferrocenecarboxaldehyde, and *N*,*N*,*N*′,*N*′-tetramethylethylenediamine (TMEDA) were obtained from Thermo Scientific. Hydrochloric acid aqueous solution (37 wt%) was purchased from Honeywell. 2-Bromoanthracene and ammonium hexafluorophosphate (NH_4PF_6) were purchased from Combi. Sodium borohydride ($NaBH_4$) and lithium aluminum hydride ($LiAlH_4$) were purchased from Alfa Aesar. Anhydrous methanol, ethanol, and tetrahydrofuran (THF) were purchased from Sigma-Aldrich in Sure/Seal containers and stored under nitrogen atmosphere. Samples were purified by medium-pressure liquid chromatography (NextGen 300+, EZ Prep), flash column chromatography, solvent flushing, and bi-solvent recrystallization.

^{1}H NMR spectra were recorded on a Bruker Avance 500 MHz spectrometer. Chemical shifts were referenced to acetone (δ = 2.05 ppm), acetonitrile (δ = 1.93 ppm), or $CDCl_3$ (δ = 7.26 ppm). High-resolution (HR) field-desorption (FD) mass spectrometry (MS) was carried out using a JEOL JMS-T200GC AccuTOF GCx instrument. Anion detection was performed by HPLC/MS-MS, using a VARIAN system (ProStar 210 Solvent Delivery Module, ProStar 410 AutoSampler, ProStar 335 Photodiode Array Detector) coupled with a VARIAN 901-MS (FT-ICR mass spectrometer). UV-vis absorption spectra were recorded using a JASCO V-630 spectrophotometer. Fluorescence spectra were measured using a JASCO FP-8500 spectrofluorometer.

4.2. Synthesis of ferrocene carbaldehyde oxime

Ferrocenecarboxaldehyde (1.00 g, 4.67 mmol, 1.0 eq.) was dissolved in ethanol (70 mL) in a 250 mL Schlenk tube. Sodium acetate (CH_3COONa, 1.95 g, 16.3 mmol, 3.5 eq.) was dissolved in water and slowly added to the Schlenk tube. After the mixture was thoroughly combined, hydroxylamine hydrochloride (650 mg, 9.34 mmol, 2.0 eq.) was added gradually. The resulting mixture was stirred at 50 °C for 4 h. Upon cooling to room temperature, the reaction mixture was quenched with water, and completion of quenching was confirmed using pH test paper. The mixture was extracted three times with CH_2Cl_2. The combined organic layers were dried over anhydrous $MgSO_4$, filtered, and the solvent was removed under reduced pressure using a rotary evaporator. The crude product, ferrocene carbaldehyde oxime, was obtained as a dark red solid (1.20 g, 4.40 mmol, 94% yield). Due to minimal byproduct formation, further purification was not required. Thin-layer chromatography using a 9 : 1 mixture of CH_2Cl_2 and ethyl acetate as the eluent showed two distinct spots (R_f = 0.33 and 0.50), attributed to the presence of stereoisomers. ^{1}H NMR (500 MHz, $CDCl_3$): δ 7.94 (s, 1H, CH═N), 4.49–4.50 (m, 2H, Cp), 4.32–4.35 (m, 2H, Cp), 4.18–4.19 (m, 5H, Cp).

4.3. Synthesis of ferrocene methylamine

$LiAlH_4$ (1.00 g, 26.4 mmol, 6.0 eq.) was placed in a double-neck round-bottom flask under a nitrogen atmosphere. Ferrocene carbaldehyde oxime (1.20 g, 4.40 mmol, 1.0 eq.) was dissolved in dry THF (60 mL) and slowly added to the flask. The reaction mixture was stirred and refluxed at 70 °C for 5 h. After cooling to room temperature, the reaction was quenched with water under an ice bath to control exothermicity. The resulting lithium salts were removed by suction filtration. The aqueous phase was extracted three times with CH_2Cl_2. The combined organic layers were dried over anhydrous $MgSO_4$, filtered, and the solvent was removed under reduced pressure using a rotary evaporator. Ferrocenemethylamine was obtained as a dark orange oil (832 mg, 3.87 mmol, 88% yield). ^{1}H NMR (500 MHz, $CDCl_3$): δ 3.53 (s, 2H, CH_2), 4.09–4.10 (m, 2H, Cp), 4.12 (m, 5H, Cp), 4.14–4.15 (m, 2H, Cp).

4.4. Synthesis of anthracene-2-carbaldehyde

In a Schlenk tube, 2-bromoanthracene (1.00 g, 3.89 mmol, 1.0 eq.) was dissolved in diethyl ether (40 mL) and sonicated for 3 min. TMEDA (2.71 g, 23.3 mmol, 6.0 eq.) was then added, and the mixture was cooled to −70 °C for 3 min. *n*-BuLi (1.99 g, 31.1 mmol, 8.0 eq.) was added dropwise under stirring. After the addition of *n*-BuLi, the reaction mixture was allowed to warm to room temperature and stirred for 2 h. The flask was then cooled in an ice bath, and DMF (5.69 g, 77.8 mmol, 20.0 eq.) was added dropwise. Stirring continued for an additional 5 h at room temperature. Upon completion, the reaction was quenched with hydrochloric acid solution, and complete quenching was confirmed using pH test paper. The mixture was extracted three times with CH_2Cl_2. The combined organic layers were dried over anhydrous $MgSO_4$, filtered, and concentrated under reduced pressure. The crude product was purified by silica gel column chromatography (hexane : CH_2Cl_2 = 1 : 1) to afford anthracene-2-carbaldehyde as a yellow powder (352 mg, 1.70 mmol, 44% yield). ^{1}H NMR (500 MHz, $CDCl_3$): δ 7.52–7.57 (m, 2H), 7.88–7.90 (d, 1H, J = 9 Hz), 8.02–8.04 (d, 1H, J = 9 Hz), 8.05–8.06 (d, 2H, J = 9 Hz), 8.45 (s, 1H), 8.49 (s, 1H), 8.61 (s, 1H), 10.17 (s, 1H, CHO).

4.5. Synthesis of A1

Ferrocenemethylamine (832 mg, 3.87 mmol, 2.5 eq.) and anthracene-2-carbaldehyde (319 mg, 1.55 mmol, 1.0 eq.) were

dissolved in a 1 : 1 mixture of THF and ethanol (100 mL), and 3 Å molecular sieves were added. The reaction mixture was stirred at 50 °C for 48 h. After the reaction, the molecular sieves were removed by suction filtration. The filtrate was extracted three times with CH_2Cl_2. The combined organic layers were dried over anhydrous $MgSO_4$, filtered, and concentrated under reduced pressure to yield a mixture of ferrocenemethylamine and the imine intermediate. This mixture was dissolved in methanol (62 mL), and $NaBH_4$ (935 mg, 24.8 mmol, 16 eq.) was slowly added. The reaction was stirred at room temperature for 7 h. Then, 6 N hydrochloric acid (3.8 mL, 6.0 eq.) was added dropwise and stirring continued for 1 h at room temperature. The reaction was quenched with water and extracted three times with CH_2Cl_2. The resulting aqueous layer contained protonated ferrocenemethylamine, while the organic layer contained ferrocenyl–anthryl ammonium chloride. The organic layer was dried over $MgSO_4$ and the solvent was removed under reduced pressure to afford [ferrocenyl–anthryl ammonium]$^+$Cl$^-$ as a crude product (358 mg, 0.81 mmol, 52.4%). The crude [ferrocenyl–anthryl ammonium]$^+$Cl$^-$ was dissolved in acetone (40 mL), and NH_4PF_6 (579 mg, 4.05 mmol, 5 eq.) was added. The mixture was stirred at room temperature for 2 h and extracted three times with CH_2Cl_2. The combined organic layers were dried over $MgSO_4$ and concentrated under reduced pressure. The resulting residue was washed with diethyl ether (15 mL) and toluene (3 mL) to yield **A1** as a brown powder (209 mg, 0.38 mmol, 47%). ^{1}H NMR (500 MHz, CD_3CN): δ 3.99 (s, 2H, CH_2), 4.19 (s, 5H, Cp), 4.23–4.24 (s, 2H, Cp), 4.25 (s, 2H, CH_2), 4.36–4.37 (m, 2H, Cp), 7.48–7.50 (d, 1H, J = 9 Hz), 7.52–7.55 (m, 2H), 8.06–8.11 (m, 4H), 8.54 (s, 2H). HRMS (FD): calcd for $C_{26}H_{24}FeN$ [M]$^+$: 406.1252, found: m/z 406.1249 (error 0.74 ppm). HRMS (ESI): calcd for PF_6^- [M]$^-$: 144.9642, found: m/z 144.9642 (error 0.07 ppm).

4.6. Synthesis of PR1

A1 (50.0 mg, 0.0907 mmol, 1.0 eq.) and DB24C8 (48.8 mg, 0.1088 mmol, 1.2 eq.) were dissolved in acetone : CH_2Cl_2 (2 mL, 51 : 49 v/v) and stirred at room temperature for 4 h. After basic filtration to remove insoluble impurities, the resulting solution was transferred to a small vial and placed inside a larger container filled with diethyl ether for vapor diffusion recrystallization over 2 days. Yellow single crystals of **PR1** were obtained. ^{1}H NMR (500 MHz, CD_3CN): δ = 3.63–3.65 (m, 8H, OCH_2), 3.77–3.79 (m, 8H, OCH_2), 3.97 (s, 2H, CH_2), 4.12–4.15 (m, 8H, OCH_2), 4.20–4.21 (s, 5H, Cp), 4.29 (s, 2H, CH_2), 4.31 (s, 2H, CH_2), 4.40 (s, 2H, Cp), 6.93–6.99 (m, 8H, aromatic H), 7.46–7.48 (d, 1H, J = 9 Hz, aromatic H), 7.53–7.56 (m, 2H, aromatic H), 8.07–8.14 (m, 4H, aromatic H), 8.56 (s, 2H, aromatic H). HRMS (FD): calcd for $C_{26}H_{24}FeN$ [M]$^+$: 406.1252, found: m/z 406.1249 (error 0.74 ppm).

4.7. Single-crystal X-ray crystallography

Single-crystal X-ray crystallography of the **PR1** was carried out using Rigaku XtaLAB Synergy-DW system. The crystallographic data of **PR1**, **PR2** and **A1** have been deposited with the CCDC under deposition number CCDC 2452984, 1500708 and 2142250.

4.8. Film preparation and characterization

Single crystals of **PR1** were ground and dispersed in 300 μL of a PBMA solution in diethyl ether. The concentration of **PR1** in PBMA was adjusted to 7 mol% (34.8 wt%), as summarized in Table S7 (ESI†). The dispersion was cast onto a PTFE film placed on a glass slide and allowed to dry. The resulting film was sandwiched between another PTFE film and a 70 μm spacer, followed by hot pressing at 50 °C. After molding, the film was peeled off, cut into 1 × 1 mm^2 pieces, and designated as **Cr.PR1-PBMA**. A PBMA film containing crystalline **PR2** (**Cr.PR2-PBMA**) was also prepared using the same procedure. Additionally, a film referred to as **PR1-PBMA** was fabricated by casting a cosolvent mixture of chloroform and acetone containing **A1**, DB24C8, and PBMA in a molar ratio of 7 : 7 : 86 (19 : 16 : 65 wt%).

XRD measurements of the PBMA films were carried out using a powder X-ray diffractometer (D2 Phaser; Bruker, Karlsruhe, Germany) with Cu-Kα radiation (λ = 1.5406 Å), operated at 30 kV and 10 mA. SEM was conducted using a Hitachi SU8010 to investigate the surface morphology of the films. Elemental composition and mapping were obtained using an energy-dispersive X-ray spectroscopy (EDS) system (Oxford Instruments X-MaxN 6857) coupled to the SEM, operated at an accelerating voltage of 15 kV. Dynamic mechanical analysis (DMA) was performed using a DMA Q800 instrument (TA Instruments) to evaluate the viscoelastic properties of the films.

4.9. Photoirradiation experiments

Photoinduced mechanical motions of crystals and free-standing PBMA films were observed using an optical microscope (Olympus BX51) equipped with a temperature-controlled stage (HCS302-mk100U and HCS302 heating/cooling unit) and a CCD camera (DFK 51AU02). Continuous-wave diode-pumped solid-state lasers emitting at 445 nm (TAN-YU, LSR445FP-1W) and 375 nm (MDL-D-375-800 mW) were used as the irradiation sources. The laser light was delivered *via* a multi-optical fiber cable and collimated using an SMA 905 collimator (for the 445 nm laser) or an FC/PC collimator (for the 375 nm laser). Laser power was adjusted by controlling the current from the respective controllers and measured using a power meter (Ophir, Nova II, P/N 7Z01550). Side-view images and videos of deformation behavior were captured using a Lumenera INFINITY 1-3C digital camera and analyzed with INFINITY ANALYZE software.

Deformation analysis was performed using ImageJ software. The height change was analyzed using a Python program built with OpenCV (cv2) and NumPy. Each video frame was processed individually. Every frame was first converted to grayscale (using cv2.cvtColor), then binarized into black and white using a fixed threshold (cv2.threshold). To reduce noise and make the shapes clearer, morphological operations (cv2.morphologyEx and cv2.dilate) were applied. A specific region in the image (*i.e.*, the actuator position) was selected, and the highest white pixel in that area was found using np.argmax. The movement was calculated by comparing this highest point to the one in the first frame (first_highest_position–highest_position), and the value was converted to millimeters using a known scale factor.

The dimensions of crystals and films were measured with a confocal laser microscope (Keyence VK9500) using a 10× objective lens. Photoinduced mechanical force was measured using the same microscope system equipped with a microforce detector module (CHIEF SI, μ-force) operated *via* Bridge DAQ software. The force detection module consisted of a cantilever with strain gauges mounted on both sides to detect small forces. All measurements were conducted on a vibration-isolated optical table to minimize external disturbances. Thermal imaging under photoirradiation was carried out using an infrared thermal imaging camera (UTI-260B).

Conflicts of interest

There are no conflicts to declare.

Data availability

The data supporting the findings of this study are available as follows: Crystallographic data for compounds **PR1**, **PR2** and **A1** have been deposited at the Cambridge Crystallographic Data Centre (CCDC) under the accession numbers CCDC 2452984, 1500708 and 2142250, respectively. All other data, including raw experimental data, spectral data, and analysis scripts used for photomechanical actuation characterization, are available in the ESI.†

Acknowledgements

This work was financially supported by Ministry of Science and Technology Taiwan (110-2221-E-007-006-MY3 and 110-2113-M-007-013-MY3) and Japan Society for the Promotion of Science (JSPS) Grant-in-Aid for Research Start-up for Returnees (24K23944).

References

1 M. Horie and C.-H. Wang, *Mater. Chem. Front.*, 2019, **3**, 2258–2269.
2 C.-H. Wang and M. Horie, *Mater. Today Chem.*, 2022, **24**, 100852.
3 S. Krause and B. L. Feringa, *Nat. Rev. Chem.*, 2020, **4**, 550–562.
4 A. Mondal, R. Toyoda, R. Costil and B. L. Feringa, *Angew. Chem., Int. Ed.*, 2022, **61**, e202206631.
5 L. Zhang, Y. Qiu, W.-G. Liu, H. Chen, D. Shen, B. Song, K. Cai, H. Wu, Y. Jiao and Y. Feng, *Nature*, 2023, **613**, 280–286.
6 W. M. Awad, D. W. Davies, D. Kitagawa, J. M. Halabi, M. B. Al-Handawi, I. Tahir, F. Tong, G. Campillo-Alvarado, A. G. Shtukenberg, T. Alkhidir, Y. Hagiwara, M. Almehairbi, L. F. Lan, S. Hasebe, D. P. Karothu, S. Mohamed, H. Koshima, S. Kobatake, Y. Diao, R. Chandrasekar, H. Y. Zhang, C. C. Sun, C. Bardeen, R. O. Al-Kaysi, B. Kahr and P. Naumov, *Chem. Soc. Rev.*, 2023, **52**, 3098–3169.
7 L. Zhang, H. Wu, X. Li, H. Chen, R. D. Astumian and J. F. Stoddart, *Nat. Rev. Methods Primers*, 2024, **4**, 13.
8 F. Nishino, P. Krüger, C. H. Wang, R. Nemoto, Y. H. Chang, T. Hosokai, Y. Hasegawa, K. Fukutani, S. Kera, M. Horie and T. K. Yamada, *Small*, 2025, **21**, 2408217.
9 S. Corra, M. Curcio, M. Baroncini, S. Silvi and A. Credi, *Adv. Mater.*, 2020, **32**, 1906064.
10 J.-S. Geng, L. Mei, Y.-Y. Liang, L.-Y. Yuan, J.-P. Yu, K.-Q. Hu, L.-H. Yuan, W. Feng, Z.-F. Chai and W.-Q. Shi, *Nat. Commun.*, 2022, **13**, 2030.
11 G. Liu, J. Zhu, Y. Zhou, Z. Dong, X. Xu and P. Mao, *Org. Lett.*, 2018, **20**, 5626–5630.
12 H.-G. Fu, Y. Chen and Y. Liu, *ACS Appl. Mater. Interfaces*, 2019, **11**, 16117–16122.
13 P. Q. Nhien, J.-H. Tien, T. T. K. Cuc, T. M. Khang, N. T. Trung, C.-H. Wu, B. Thi Buu Hue, J. I. Wu and H.-C. Lin, *J. Mater. Chem. C*, 2022, **10**, 18241–18257.
14 L. M. Zhao, L. S. Zheng, X. Wang and W. Jiang, *Angew. Chem., Int. Ed.*, 2022, **61**, e202214296.
15 X. Ge, Y. He, X. Liang, L. Wu, Y. Zhu, Z. Yang, M. Hu and T. Xu, *Nat. Commun.*, 2018, **9**, 2297.
16 Q. y Jin, L. Meng, Z. h Zhang, Y. y Liang, W. Jin, K. q Hu, L. y Yuan, Z. F. Chai, L. Mei and W. q Shi, *Adv. Funct. Mater.*, 2023, **33**, 2303530.
17 V. García-López, F. Chen, L. G. Nilewski, G. Duret, A. Aliyan, A. B. Kolomeisky, J. T. Robinson, G. Wang, R. Pal and J. M. Tour, *Nature*, 2017, **548**, 567–572.
18 F. Lancia, A. Ryabchun and N. Katsonis, *Nat. Rev. Chem.*, 2019, **3**, 536–551.
19 C. Biagini and S. Di Stefano, *Angew. Chem.*, 2020, **132**, 8420–8430.
20 C. Cheng, P. R. McGonigal, S. T. Schneebeli, H. Li, N. A. Vermeulen, C. Ke and J. F. Stoddart, *Nat. Nanotechnol.*, 2015, **10**, 547–553.
21 Y. Feng, M. Ovalle, J. S. Seale, C. K. Lee, D. J. Kim, R. D. Astumian and J. F. Stoddart, *J. Am. Chem. Soc.*, 2021, **143**, 5569–5591.
22 C. Zazza, S. Borocci and N. Sanna, *Phys. Chem. Chem. Phys.*, 2024, **26**, 5399–5407.
23 A. Colin-Molina, D. P. Karothu, M. J. Jellen, R. A. Toscano, M. A. Garcia-Garibay, P. Naumov and B. Rodríguez-Molina, *Matter*, 2019, **1**, 1033–1046.
24 I. Liepuoniute, M. J. Jellen and M. A. Garcia-Garibay, *Chem. Sci.*, 2020, **11**, 12994–13007.
25 E. Moulin, L. Faour, C. C. Carmona-Vargas and N. Giuseppone, *Adv. Mater.*, 2020, **32**, 1906036.
26 T. Uchikura, M. Oshima, M. Kawasaki, K. Takahashi and N. Iwasawa, *Angew. Chem., Int. Ed.*, 2020, **59**, 7403–7408.
27 W. Cho, J. Jeon, W. Eom, J. G. Lee, D. G. Kim, Y. S. Kim, T. H. Han and J. J. Wie, *Adv. Funct. Mater.*, 2021, **31**, 2102106.
28 J. M. Abendroth, O. S. Bushuyev, P. S. Weiss and C. J. Barrett, *ACS Nano*, 2015, **9**, 7746–7768.
29 M. E. Howe and M. A. Garcia-Garibay, *J. Org. Chem.*, 2019, **84**, 9835–9849.
30 M. Jin, S. Yamamoto, T. Seki, H. Ito and M. A. Garcia-Garibay, *Angew. Chem., Int. Ed.*, 2019, **58**, 18003–18010.
31 D. Kitagawa, H. Tsujioka, F. Tong, X. Dong, C. J. Bardeen and S. Kobatake, *J. Am. Chem. Soc.*, 2018, **140**, 4208–4212.

32 H. Liu, Z. Lu, B. Tang, C. Qu, Z. Zhang and H. Zhang, *Angew. Chem.*, 2020, **132**, 13044–13050.
33 Y. Yao, L. Zhang, E. Orgiu and P. Samorì, *Adv. Mater.*, 2019, **31**, 1900599.
34 N. Grabicki, O. Dumele, H. Sai, N. E. Powers-Riggs, B. T. Phelan, M. H. Sangji, C. T. Chapman, J. V. Passarelli, A. J. Dannenhoffer and M. R. Wasielewski, *Chem. Mater.*, 2021, **33**, 706–718.
35 S. D. Karlen, H. Reyes, R. Taylor, S. I. Khan, M. F. Hawthorne and M. A. Garcia-Garibay, *Proc. Natl. Acad. Sci. U. S. A.*, 2010, **107**, 14973–14977.
36 A. Hasija, A. J. Thompson, L. Singh, S. N. Megha, K. S. Mangalampalli, J. C. McMurtrie, M. Bhattacharjee, J. K. Clegg and D. Chopra, *Small*, 2023, **19**, 2206169.
37 T. Pan and J. Liu, *ChemPhysChem*, 2016, **17**, 1752–1758.
38 L. van Dijk, M. J. Tilby, R. Szpera, O. A. Smith, H. A. Bunce and S. P. Fletcher, *Nat. Rev. Chem.*, 2018, **2**, 0117.
39 L. Catalano and P. Naumov, *CrystEngComm*, 2018, **20**, 5872–5883.
40 M. Horie, Y. Suzaki, D. Hashizume, T. Abe, T. D. Wu, T. Sassa, T. Hosokai and K. Osakada, *J. Am. Chem. Soc.*, 2012, **134**, 17932–17944.
41 K.-J. Chen, Y.-C. Tsai, Y. Suzaki, K. Osakada, A. Miura and M. Horie, *Nat. Commun.*, 2016, **7**, 13321.
42 S.-C. Cheng, K.-J. Chen, Y. Suzaki, Y. Tsuchido, T.-S. Kuo, K. Osakada and M. Horie, *J. Am. Chem. Soc.*, 2018, **140**, 90–93.
43 S.-C. Cheng, C.-H. Wang, Y.-C. Lin, Y. Tsuchido, Y. Suzaki, Y. Sei, T.-S. Kuo and M. Horie, *ACS Appl. Mater. Interfaces*, 2020, **12**, 50002–50010.
44 C.-H. Wang, Y.-C. Lin, S. Bhunia, Y. Feng, P. Kundu, C. L. Stern, P.-L. Chen, J. F. Stoddart and M. Horie, *J. Am. Chem. Soc.*, 2023, **145**, 21378–21386.
45 C.-H. Wang, K.-J. Chen, T.-H. Wu, H.-K. Chang, Y. Tsuchido, Y. Sei, P.-L. Chen and M. Horie, *Chem. Sci.*, 2021, **12**, 3871–3875.
46 H. Lim, S. J. Woo, Y. H. Ha, Y. H. Kim and J. J. Kim, *Adv. Mater.*, 2022, **34**, 2100161.
47 L. Xing, Z.-L. Zhu, J. He, Z. Qiu, Z. Yang, D. Lin, W.-C. Chen, Q. Yang, S. Ji and Y. Huo, *J. Chem. Eng.*, 2021, **421**, 127748.
48 X. Zeng, D. Zhang, Y. Zhu, M. Chen, H. Chen, S. Kasai, H. Meng and O. Goto, *J. Mater. Chem. C*, 2019, **7**, 14275–14283.
49 M. Chen, L. Yan, Y. Zhao, I. Murtaza, H. Meng and W. Huang, *J. Mater. Chem. C*, 2018, **6**, 7416–7444.
50 T. Salzillo and A. Brillante, *CrystEngComm*, 2019, **21**, 3127–3136.
51 K. Yuhara and K. Tanaka, *Angew. Chem.*, 2024, **63**, e202319712.
52 J. Zhong, J. Sun, K. Ye and R. Lu, *J. Mater. Chem. C*, 2023, **11**, 16452–16472.
53 C. J. Perry and G. J. Beran, *Cryst. Growth Des.*, 2023, **23**, 8352–8360.
54 Y. Sagara, M. Karman, A. Seki, M. Pannipara, N. Tamaoki and C. Weder, *ACS Cent. Sci.*, 2019, **5**, 874–881.
55 S. Teka, A. Jebnouni, M. Chemli, G. Attia, Z. Baatout, N. S. Jaballah, M. Ghorbel and M. Majdoub, *J. Mol. Struct.*, 2023, **1289**, 135802.
56 A. Garci, Y. Beldjoudi, M. S. Kodaimati, J. E. Hornick, M. T. Nguyen, M. M. Cetin, C. L. Stern, I. Roy, E. A. Weiss and J. F. Stoddart, *J. Am. Chem. Soc.*, 2020, **142**, 7956–7967.
57 C.-H. Wang, H.-K. Chang, K.-J. Chen, D.-H. Huang, C.-J. Chang, K.-H. Huang, Y.-D. Chiu and M. Horie, *ACS Appl. Mater. Interfaces*, 2023, **15**, 38846–38856.
58 C. Song, Y. Zhang, J. Bao, Z. Wang, L. Zhang, J. Sun, R. Lan, Z. Yu, S. Zhu and H. Yang, *Adv. Funct. Mater.*, 2023, **33**, 2213771.
59 M. Li, A. Pal, A. Aghakhani, A. Pena-Francesch and M. Sitti, *Nat. Rev. Mater.*, 2022, **7**, 235–249.
60 I. Apsite, S. Salehi and L. Ionov, *Chem. Rev.*, 2021, **122**, 1349–1415.
61 Z. Han, P. Wang, G. Mao, T. Yin, D. Zhong, B. Yiming, X. Hu, Z. Jia, G. Nian and S. Qu, *ACS Appl. Mater. Interfaces*, 2020, **12**, 12010–12017.
62 Y. Yang, E. M. Terentjev, Y. Zhang, Q. Chen, Y. Zhao, Y. Wei and Y. Ji, *Angew. Chem., Int. Ed.*, 2019, **58**, 17474–17479.
63 B. Zhou, Y. Li, G. Niu, M. Lan, Q. Jia and Q. Liang, *ACS Appl. Mater. Interfaces*, 2016, **8**, 29899–29905.
64 B. Guo, Z. Sheng, D. Hu, C. Liu, H. Zheng and B. Liu, *Adv. Mater.*, 2018, **30**, 1802591.
65 Y. Jiang, J. Li, X. Zhen, C. Xie and K. Pu, *Adv. Mater.*, 2018, **30**, 1705980.
66 H.-K. Chang, C.-C. Huang, P.-R. Wu, K.-H. Lin and M. Horie, *Mater. Today Chem.*, 2025, **45**, 102663.
67 A. van Der Lee and D. G. Dumitrescu, *Chem. Sci.*, 2021, **12**, 8537–8547.
68 T. J. Jacobsson, L. J. Schwan, M. Ottosson, A. Hagfeldt and T. Edvinsson, *Inorg. Chem.*, 2015, **54**, 10678–10685.
69 P. R. Spackman, M. J. Turner, J. J. McKinnon, S. K. Wolff, D. J. Grimwood, D. Jayatilaka and M. A. Spackman, *J. Appl. Crystallogr.*, 2021, **54**, 1006–1011.
70 M. Ashfaq, K. S. Munawar, M. N. Tahir, N. Dege, M. Yaman, S. Muhammad, S. S. Alarfaji, H. Kargar and M. U. Arshad, *ACS Omega*, 2021, **6**, 22357–22366.
71 L. H. Al-Wahaibi, J. Joubert, O. Blacque, N. H. Al-Shaalan and A. A. El-Emam, *Sci. Rep.*, 2019, **9**, 19745.
72 H. Aziz, A. Saeed, C. J. McAdam, J. Simpson, T. Hökelek, E. Jabeen, A. Khurshid, M. Saleem and H. R. El-Seedi, *J. Mol. Struct.*, 2023, **1281**, 135108.
73 N. Tyagi, N. Sinha, H. Yadav and B. Kumar, *RSC Adv.*, 2016, **6**, 24565–24576.
74 F. Liu, Z. Cheng, L. Wan, L. Gao, Z. Yan, D. Hu, L. Ying, P. Lu and Y. Ma, *J. Chem. Eng.*, 2021, **426**, 131351.
75 R. Yao, L. Zhong, Y. Han, C. Jin, J. Lu, F. Chen, L. Liao, Z. Chen, Y. Zhang and G. Chen, *J. Phys. Chem. C*, 2020, **124**, 8885–8893.
76 M. C. Drummer, V. Singh, N. Gupta, J. L. Gesiorski, R. B. Weerasooriya and K. D. Glusac, *Photosynth. Res.*, 2022, **151**, 163–184.
77 H. Niu, J. Liu, H. M. O'Connor, T. Gunnlaugsson, T. D. James and H. Zhang, *Chem. Soc. Rev.*, 2023, **52**, 2322–2357.
78 B. Wang, G. Feng, M. Seifrid, M. Wang, B. Liu and G. C. Bazan, *Angew. Chem., Int. Ed.*, 2017, **56**, 16063–16066.
79 H. Li, L. Li, Y. Sha, Y. Lu, C. Teng, D. Zhou, W. Chen and G. Xue, *Polymers*, 2022, **14**, 1652.
80 K.-J. Chen, P.-L. Chen and M. Horie, *Sci. Rep.*, 2017, **7**, 14195.
81 K.-J. Chen, A. C. Tan, C.-H. Wang, T.-S. Kuo, P.-L. Chen and M. Horie, *Cryst. Growth Des.*, 2018, **19**, 17–22.

